JMEPEG (2018) 27:4107–4114
https://doi.org/10.1007/s11665-018-3474-8

1059-9495/$19.00

Formation and Toughening Mechanisms of Dispersions in Interfacial Intermetallics of Dissimilar Laser Al/Steel Joints

J. Yang, Z.S. Yu, Y.L. Li, H. Zhang, W. Guo, P. Peng, and Y.N. Zhou

(Submitted November 3, 2017; in revised form March 8, 2018; published online June 29, 2018)

The key to improve the strength of Al/steel dissimilar joint is to toughen the hard and brittle interfacial intermetallics. Introducing soft and tough dispersions into the interfacial intermetallics would be a promising method. In the present study, Zn-Al alloy (Zn-22Al) was used as the filler metal to generate dispersions in the interfacial intermetallics matrix of dissimilar laser Al/steel joint. The results have shown that soft and tough dispersions, i.e., $FeZn_{10}$, Al-rich amorphous phase, and Zn solid solution, were successfully introduced into the hard and brittle $Fe_2Al_{5-x}Zn_x$ matrix. The formation of these dispersions was resulted from diffusion of elements Fe and Al and infiltration of liquid Zn along the grain boundaries of $Fe_2Al_{5-x}Zn_x$ matrix and the subsequent chemical reaction and solidification. With this kind of interfacial microstructure, the joint exhibited a stable peak fracture load of 1200 N even though the interfacial layer thickness increased from 20 to 45 μm. This was because the interfacial layer was toughened by the soft and tough dispersions. Using this example, introduction of soft and tough dispersions into hard and brittle intermetallics matrix to toughen interfacial layer and then strengthening of dissimilar joints will be highlighted.

Keywords dispersion toughening, dissimilar materials, grain boundary, interfacial microstructure, intermetallics, laser welding

1. Introduction

Since reducing the weight of automotive components is one of efficient countermeasures against greenhouse gas emissions, light-weight aluminum alloys have been increasingly applied in the fabrication of the vehicles due to their high strength-to-weight ratio, good machinability, environmental friendliness, and recyclability. Additionally, high-strength steel with good durability is also a very promising structural material in vehicle applications. To achieve the comprehensive excellent properties of Al alloys and high-strength steel, the development of reliable Al/steel dissimilar joints is necessary. However, the formation of hard and brittle Fe-Al intermetallics (IMCs) can significantly decrease the joint strength which is due to their low critical stress intensity factor and high crack propagation rate (Ref 1-3). To achieve a reliable welding of these two materials, some novel welding technologies, such as ultrasonic welding (Ref 4, 5), vaporizing foil actuator welding (Ref 6), friction stir welding (Ref 7-9), explosion welding (Ref 10), laser joining (Ref 11-17), were explored.

Laser joining is regarded as a desirable method for joining of Al/steel dissimilar materials due to its high energy density, high heating/cooling rates, and high processing speed. As a result of short metallurgical reaction time, the formation of hard and brittle IMCs can be suppressed efficiently. For example, Sierra et al. (Ref 15) optimized the process parameters of Al/steel laser brazing with Al-Si filler metal. A 2-μm-thick interfacial layer consisting of Fe-Al-Si and Fe-Al IMCs was obtained, and the joint strength reached 190 N mm^{-1}. Mi et al. (Ref 16) reported that the morphology and type of interfacial IMCs were strongly correlated with heat input in laser welding of Al to steel. They observed that the interfacial reaction layer changed from thin reaction layer of $FeAl_3$ + Fe_2Al_5 to thick reaction layer of FeAl + $FeAl_3$ + Fe_2Al_5 with the heat input increased from 162 to 307 J/mm. The maximum fracture load reached 1.7 kN at the heat input of 162 J/mm. Tan et al. (Ref 17) investigated the effect of groove shape on the interfacial IMCs and tensile strength of dissimilar laser Al/steel joint. They indicated that half V-shape groove with smallest temperature gradient yielded a 1.0-8.6-μm-thick reaction layer of $FeAl_3$ and $Al_{7.4}Fe_{1.8}Si$ IMCs and highest joint strength of 137.2 MPa. However, according to the literatures above, even though many measures, e.g., optimizing process parameters and joint configurations as well as introducing alloy elements, were taken to modulate the interfacial IMCs, it was still only consisted of hard and brittle IMCs, such as Fe-Al and Fe-Al-Si IMCs.

Inspired by the dispersion toughening, we hypothesize that the interfacial layer is expected to be toughened if soft and tough dispersions can be introduced into the hard and brittle IMCs matrix. With the toughened interfacial layer, the resultant joint is likely to be strengthened. One of techniques to generate dispersions in matrixes is liquid metal infiltration, which is

J. Yang and **Z. S. Yu**, School of Materials Engineering, Shanghai University of Engineering Science, Shanghai 201620, China; and **Y. L. Li** and **H. Zhang**, Key Laboratory of Robot and Welding Automation of Jiangxi Province, School of Mechanical and Electrical Engineering, Nanchang University, Nanchang 330031, China; and **W. Guo** and **P. Peng**, School of Mechanical Engineering and Automation, Beihang University, Beijing 100191, China; and and **Y. N. Zhou**, Center for Advanced Materials Joining, University of Waterloo, Waterloo, ON N2L 3G1, Canada. Contact e-mail: jyang@sues.edu.cn.

infiltrating liquid low-melting-point metals (melts) into a packed metal/IMCs/ceramic matrix with or without external stress/pressure. By selecting appropriate materials (low-melting-point metals and base metals) and controlling welding heat cycles, it was possible to produce soft and tough dispersions in interfacial IMCs of dissimilar laser Al/steel joints. The objective of this paper was therefore to study the feasibility of this hypothesis. The formation mechanism of dispersions and the associated toughening mechanism were also discussed.

2. Experimental

Zn-coated DP980 steel sheet in a thickness of 1.0 mm was used in the present study. The zinc coating was obtained by hot dip galvanizing with the thickness of 10-15 μm. The Zn coating was mechanically removed before welding to exclude its influence on the interfacial microstructure. AA 5754-O aluminum alloy in a thickness of 1.5 mm was used. In the light of excellent infiltration capability along grain boundaries (GBs) (Ref 18-20), Zn-Al alloy was used as low-melting-point materials to generate dispersions in the IMCs matrix. Thus, commercial Zn-22Al filler metal with the diameter of 1.6 mm was used. The chemical compositions and mechanical properties of the materials are given in Tables 1 and 2, respectively. An anticorrosive brazing flux Superior No. 20 was used. The as-received flux powder was mixed with ethanol into a paste and then evenly sprinkled on the sample to obtain an estimated average thickness of 10-50 μm.

The DP980 steel and 5754 aluminum alloy coupons were cut to the dimensions of 50 mm × 60 mm. All specimens were sheared to size parallel to the rolling direction. Prior to welding, DP980 steel and 5754 aluminum alloy were cleaned using acetone and methanol to remove the grease. 5754 aluminum alloy was then chemically cleaned to remove the oxide layer.

Diode laser welding/brazing experiments were performed with a Nuvonyx diode laser system (maximum power of 4.0 kW) and a Panasonic six-axis robot arm. The filler metal was preset on the surface of the steel sheet. Argon shielding gas was provided to limit oxidation, with a flow rate of 15 L/min. The layout of laser welding/brazing experiment is illustrated in Fig. 1(a). The process parameters were as follows: 1.2-3.6 kW laser power, 0.3 m/min travel speed, and 90° incident angle. The laser beam was focused on top of the filler metal.

Cross sections were cut from the laser joints and mounted in phenolic resin. To reveal the microstructure, samples were then prepared with standard grinding and polishing process, and etched with Keller's reagent (1 ml HCl, 1.5 mL HNO_3, 2.5 mL HF and 95 ml H_2O) for 3-5 s. Scanning electron microscopy (SEM) was performed using a JEOL JSM-6460 equipped with Oxford INCA energy-dispersive x-ray spectrometer (EDS). Transmission electron microscopy (TEM) samples of about 15 μm × 25 μm × 0.1 μm were prepared from the cross sections using a Zeiss NVision 40 FIB (focused ion beam) with a Ga + ion. TEM was performed using a JEOL 2010F for bright field (BF) imaging, selected area diffraction (SAD) pattern and TEM-EDS analysis. SAD patterns were indexed with the aid of Gatan Digital Micrograph. X-ray diffraction

Table 1 Chemical compositions of the materials in wt.%

Materials	Mg	Cr	Mn	Si	Cu	Zn	Ti	Fe	Mo	C	Al	B
DP980 steel	…	0.15	2.1	0.05	…	…	…	Bal.	0.35	0.135	0.45	0.007
5754 Al	2.6-3.6	0.3	0.5	0.4	0.1	0.2	0.15	0.4	…	…	Bal.	…
Zn-22Al	…	…	…	…	…	Bal.	…	…	…	…	22.0	…

Table 2 Mechanical properties of the base materials

Materials	Yield strength, MPa	Ultimate strength, MPa	Elongation, %
DP980 steel	666 ± 36	1005 ± 7	12.5 ± 0.7
5754 Al	85 ± 11	239 ± 3	16.2 ± 1.3

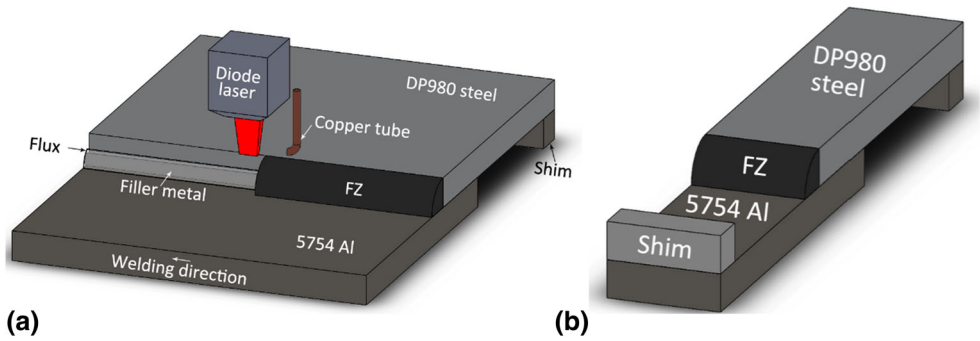

Fig. 1 Schematic description of (a) set up used in laser welding/brazing, and (b) tensile–shear test sample

(XRD) was performed by using an INEL XRG-3000 diffractometer.

Tensile test specimens were cut from the welds by the abrasive water jet technique. The specimens were evaluated by tensile–shear tests at room temperature with a crosshead speed of 1 mm/min using Instron 5548 MicroTester, in a direction perpendicular to the joining line, as shown in Fig. 1(b). Shims were used at each end of the specimens to ensure shear loads in the overlap joint while minimizing induced couples or bending of the specimens. Nanohardness of the interfacial phases was evaluated with a constant force of 4000 mN. Microindentation test was performed using a microhardness indenter with 500 g indentation force and 15 s dwell time.

3. Results

3.1 Microstructure

The typical weld appearance and cross-sectional views of laser Al/steel joint with Zn-22Al filler metal at 2.6 kW laser power and 0.3 m/min travel speed are shown in Fig. 2. A uniform fusion zone (FZ) with good wetting of both base materials and some partial melting of the Al base metal was observed.

Figure 3(a) shows the magnified backscattered electron (BSE) image of FZ/steel interface which is highlighted as a white square in Fig. 2(b). Nonhomogeneous distributed dispersions were observed in the interfacial layer (matrix). According to the microstructure, this layer was divided into two zones, i.e., zone I and zone II. In zone I, adjacent to the steel side, white blocky dispersions were observed in a dark matrix. Besides, within the white blocky dispersions, some gray lath features were seen (Fig. 3b). The dark, white, and gray structures were identified as $Fe_2Al_{5-x}Zn_x$ IMCs, $FeZn_{10}$ IMCs, and Al-rich amorphous phase, based on our previous study (Ref 21). In zone II (Fig. 3c), adjacent to the FZ side, some nanoscale light features were observed in the dark $Fe_2Al_{5-x}Zn_x$ matrix. In order to better interpret the SEM data, and to better characterize the nanoscale structures, TEM specimens were prepared at the interfacial region by FIB extraction (Fig. 4). The white dashed lines in the TEM BF image indicate the location of the nanoscale structures. It clearly shows that the structures are mostly in a film-like shape, and they connect with

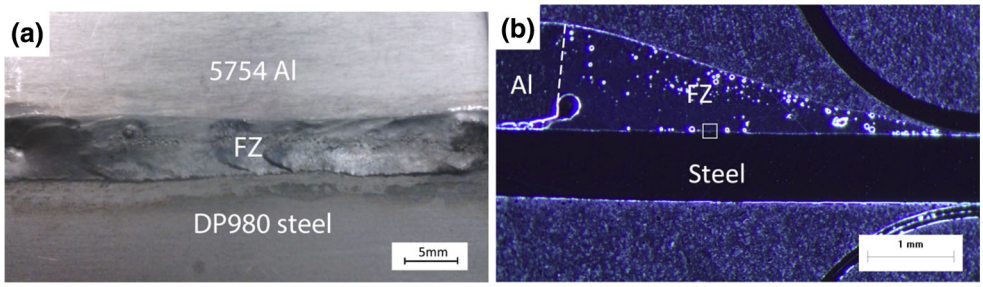

Fig. 2 Typical weld appearance and cross section of laser Al/steel joint at 2.6 kW laser power and 0.3 m/min travel speed: (a) weld appearance, and (b) cross section

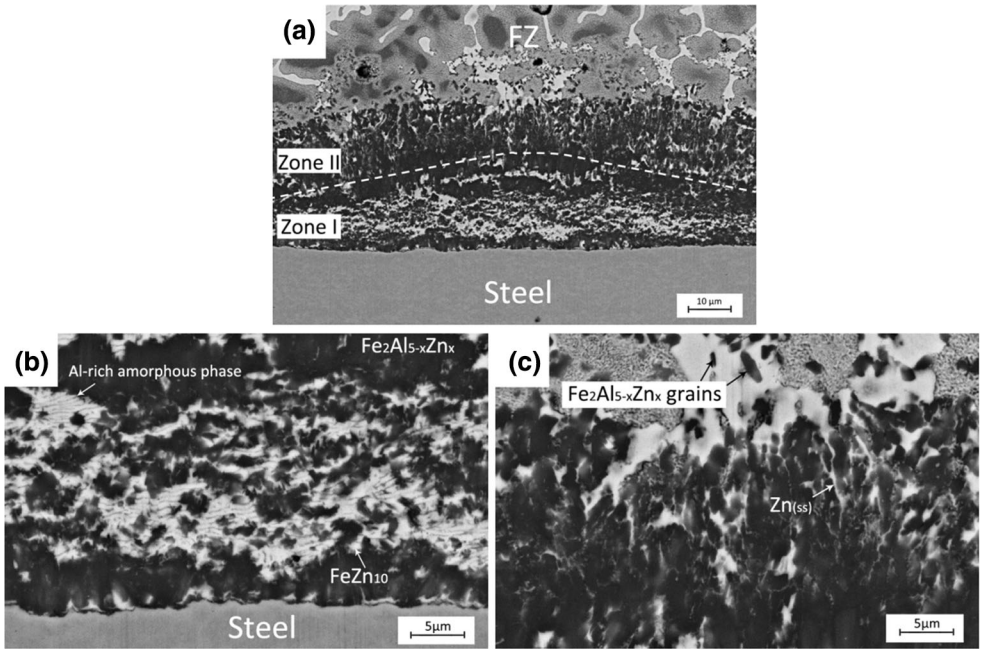

Fig. 3 BSE SEM images of microstruture at the FZ/steel interface: (a) overall view, (b) zone I, and (c) zone II

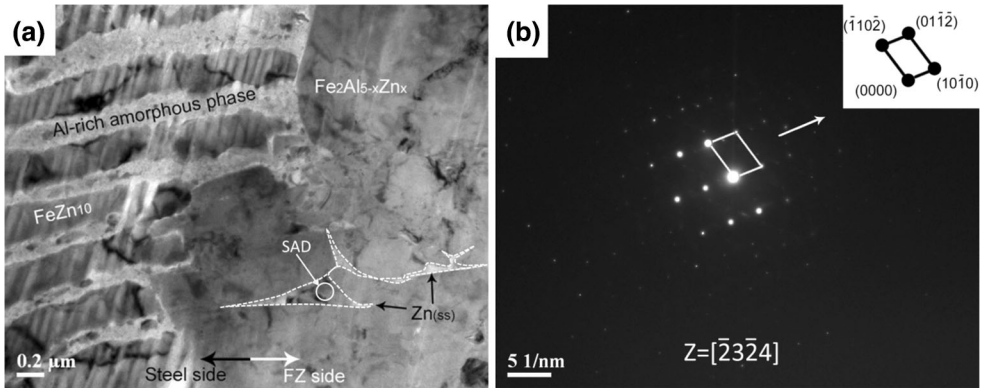

Fig. 4 TEM analysis of interfacial phases: (a) BF image, and (b) SAD pattern for $Zn_{(ss)}$ as denoted in (a)

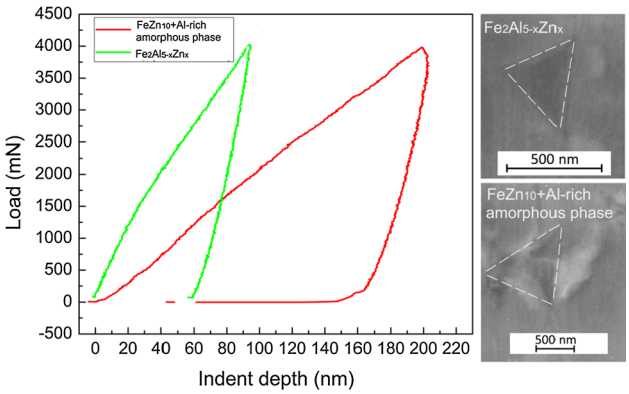

Fig. 5 Load–indent depth curve and SEM images of nanohardness indents for the interfacial phases

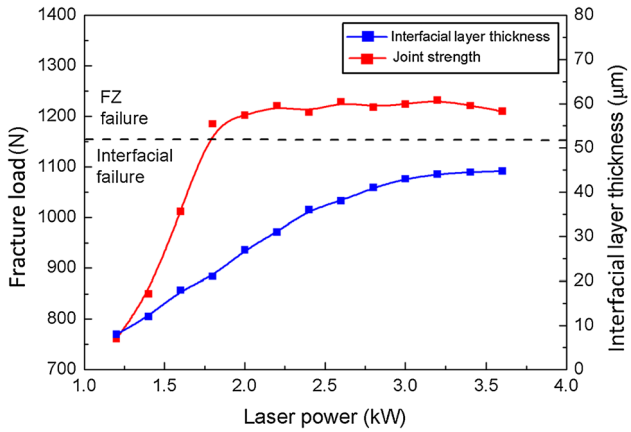

Fig. 6 Laser power vs. fracture load and interfacial layer thickness showing the joint failure modes

each other forming networks along $Fe_2Al_{5-x}Zn_x$ GBs. Typical SAD pattern of this phase found in the TEM foil shown in Fig. 4(b). It displays a standard diffraction pattern of hexagonal crystal lattice, which represents the incident beam $[\bar{2}4\bar{2}3]$. Based on TEM-EDS analysis, it had average chemical compositions of 96.0 at.% Zn, 2.7 at.% Al and 1.3 at.% Fe. Thus, the nanoscale structure was confirmed as Zn solid solution with some Al and Fe, referred to hereafter as $Zn_{(ss)}$. Considering the overall structures at the interfacial region, four different phases were formed, i.e., $Fe_2Al_{5-x}Zn_x$ matrix and dispersions including $FeZn_{10}$, Al-rich amorphous phase and $Zn_{(ss)}$. Hence, it was suggested that the target microstructure, i.e., dispersions in IMCs matrix, was produced at the interface between FZ and steel in dissimilar laser Al/steel joints.

3.2 Nanohardness and Fracture Toughness

Figure 5 shows the load–indent depth curve and SEM images of nanohardness indents. The nanohardness of $Fe_2Al_{5-x}Zn_x$ was 11.17 GPa (~ 1139 HV). Because the fine lath shape of Al-rich amorphous phase that embedded in $FeZn_{10}$ (Fig. 3b and 4a), it was difficult to measure their individual hardness. Thus, the overall nanohardness of the two phases was measured, which was around 3.08 GPa (~ 314 HV). Due to the nanoscale size and film-like shape of $Zn_{(ss)}$, it was hard to accurately measure the nanohardness. But, as a kind of solid solution, the naonhardness of $Zn_{(ss)}$ was obviously much lower than $Fe_2Al_{5-x}Zn_x$ IMCs. Besides, the fracture toughness of $FeZn_{10}$ and Fe_2Al_5 were 2 MPa $\sqrt{m}$ (Ref 22) and 1 MPa $\sqrt{m}$ (Ref 23) respectively, which indicated the fact that $FeZn_{10}$ was tougher than $Fe_2Al_{5-x}Zn_x$. Note that $Fe_2Al_{5-x}Zn_x$ was a variation of Fe_2Al_5. Moreover, $Zn_{(ss)}$ as a kind of solid solution and Al-rich amorphous phase as a kind of amorphous phase were believed to be less brittle than $Fe_2Al_{5-x}Zn_x$ IMCs. Thus, it was concluded that $FeZn_{10}$, Al-rich amorphous phase and $Zn_{(ss)}$ were all softer and tougher than $Fe_2Al_{5-x}Zn_x$.

3.3 Joint Strength

The joint strength is presented as fracture load with the unit of newton (N) as the geometry of the tensile specimens was not identical due to different FZ geometries developed in laser joining under different process conditions, and the complex stresses involved in such situations. Figure 5 plots the fracture load as a function of laser power. The fracture load gradually increased with the rising laser power (1.2-1.6 kW), and the joint failed at the FZ/steel interface. Then, a peak fracture load (~ 1200 N) was attained at laser powers of 1.8-3.6 kW, which led to an FZ failure near the Al/FZ interface.

Figure 6 also presents the relationship between the interfacial layer thickness and fracture load. The fracture load first increased when the interfacial layer thickness increased from 8

to 20 μm and kept constant when the interfacial layer thickness increased from 20 to 45 μm. This observation is in contradiction with most of previous research that a thick interfacial layer has negative effect on the joint strength especially when it is over 10 μm (Ref 8, 13, 15, 24). The discrepancy could be because the $Fe_2Al_{5-x}Zn_x$ layer is toughened by the soft and tough dispersions. The toughening mechanism will be discussed in detail later.

To investigate the relationship between fracture load and laser power, the FZ geometry was quantitatively analyzed. Contact angle and FZ width were used as the parameters to characterize the FZ geometry, as shown in Fig. 7. With the rising laser power, the contact angle gradually decreased from 32° to 13°, while the FZ width progressively increased from 3.5 to 6.5 mm. That was to say, the interfacial bonding area increased with the increasing laser power. When the laser power was ranging from 1.2 to 1.6 kW, the improved fracture load was mainly ascribed to the increased FZ/steel interfacial bonding area. When the laser power was between 1.8 and 3.6 kW, the bonding strength at the FZ/steel interface exceeded the bonding strength at the Al/FZ interface, which led to the change in failure mode from interfacial failure to FZ failure.

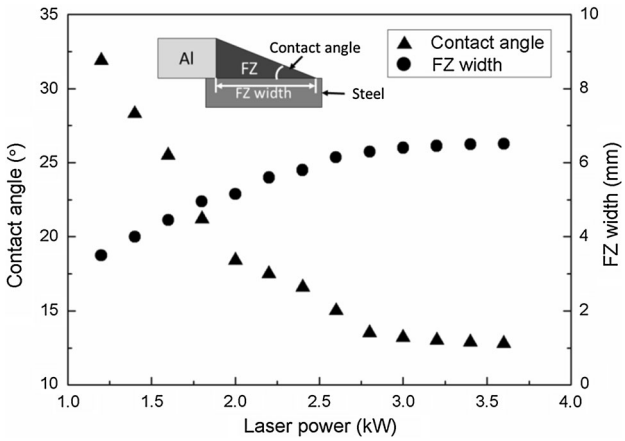

Fig. 7 Laser power vs. contact angle and FZ width showing the definition of contact angle and FZ width

3.4 Fractography

Figure 8 shows the schematic illustrations, SEM, and XRD analyses of the failure joint with interfacial failure mode. As shown in Fig. 7(b), the fracture occurred at the interface between interfacial layer and steel. Figure 8(c) presents the fracture surface of the failure joint at interfacial layer side. Dark surface and light particles were observed. Based on the EDS analysis, average chemical compositions of particles (P_1) and surface (A_1) were 8.0 at.% Al, 76.9 at.% Fe, 15.1 at.% Zn and 60.8 at.% Al, 28.2 at.% Fe, 11.0 at.% Zn, respectively. Thus, the light particles could be identified as $FeZn_{10}$, while the dark surface could be identified as $Fe_2Al_{5-x}Zn_x$, which were further confirmed by XRD analysis (Fig. 8d).

Figure 9 shows the schematic illustration and SEM analysis of the failure joint with FZ failure mode. As shown in Fig. 9(b) and (c), uniform dimples were evident on the fracture surfaces at both sides indicating a ductile failure. According to the EDS analysis, both fracture surfaces (A_2 and A_3) presented similar chemical compositions, which were around 96.9 at.% Al and 3.1 at.% Mg. Thus, it was obvious that the failure actually occurred at Al heat-affected zone (HAZ).

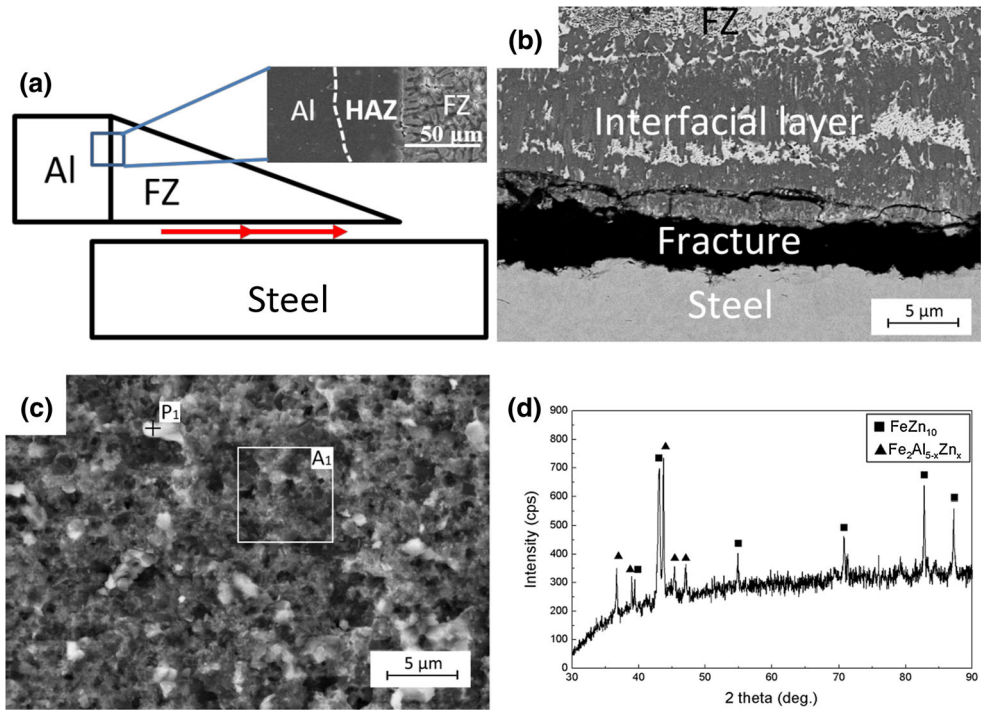

Fig. 8 Fracture surface and XRD analysis of the joint with interfacial failure mode: (a) and (b) schematic diagrams and cross section of the fracture locations showing the fracture directions by arrows, (c) SEM image of the fracture surface at the interfacial layer side, and (d) XRD patterns of the fracture surface at the interfacial layer side

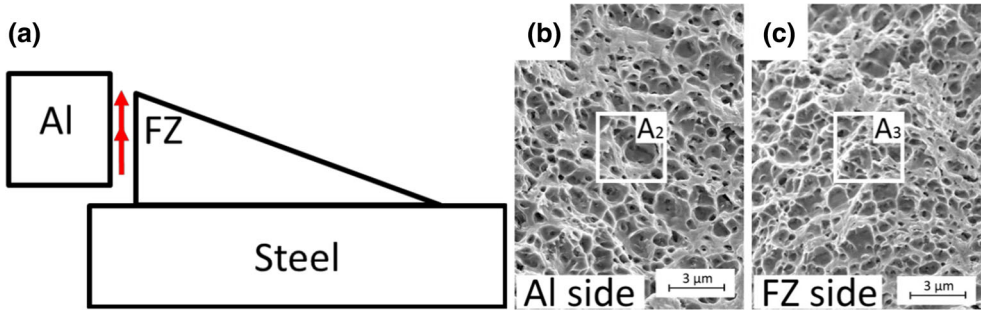

Fig. 9 Fracture surfaces and SEM analysis of the joint with FZ failure mode: (a) schematic diagrams of the fracture locations showing the fracture directions by arrows, (b) and (c) SEM images of fracture surfaces at the Al and FZ sides

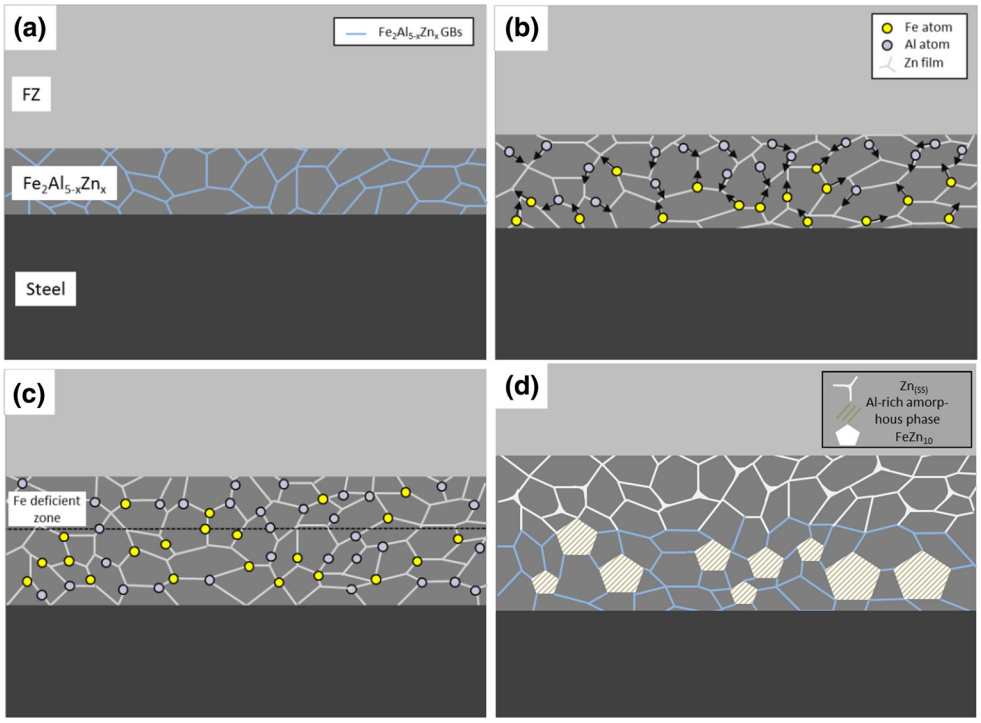

Fig. 10 Schematic illustrations of formation mechanism of the interfacial phases: (a) formation of the $Fe_2Al_{5-x}Zn_x$ matrix showing the GBs, (b) liquid Zn infiltration and Fe and Al atomic migration along $Fe_2Al_{5-x}Zn_x$ GBs (arrows indicate the moving directions of atoms), (c) formation of an Fe-deficient zone, and (d) formation of dispersions

4. Discussion

In the present study, by selecting Zn-22Al filler metal as the low-melting-point material and controlling the process parameters, soft and tough dispersions including $Zn_{(ss)}$, $FeZn_{10}$ and Al-rich amorphous phase were formed in the hard and brittle $Fe_2Al_{5-x}Zn_x$ layer of dissimilar laser Al/steel joint. To authors' best knowledge, this kind of interfacial microstructure with desirable mechanical properties has not been previously reported in dissimilar materials joining. Thus, the following discussions are mainly focus on the formation mechanism of the dispersions and the associated toughening mechanism.

4.1 Formation Mechanism

As mentioned above, by virtue of excellent infiltration capability along GBs, Zn-Al alloy was selected as the low-melting-point material to generate dispersions in interfacial IMCs matrix, of which element Zn played a dominant roll in the infiltration effect. It is well known that liquid Zn is easy to infiltrate along GBs of solid substrates, which often causes liquid–metal-induced embrittlement (Ref 25). As proposed by Smith (Ref 26), if a liquid infiltrates a polycrystalline solid, the following in equation will be satisfied $\gamma_{GB} \geq 2\gamma_{SL}$, where γ_{GB} and γ_{SL} represent interfacial tension at grain boundary and solid/liquid interface, respectively. When equilibrium state is attained, it can be given as $\gamma_{GB} = 2\gamma_{SL}\cos\left(\frac{\theta}{2}\right)$, where θ is dihedral angle. In this study, θ is believed to be 0° because $Zn_{(ss)}$ is found to continuously distributed around $Fe_2Al_{5-x}Zn_x$ grains forming networks (Fig. 3c and 4a), which suggests a complete infiltration. Thus, it is inferred that liquid Zn is theoretically able to infiltrate along the $Fe_2Al_{5-x}Zn_x$ GBs infinitely. Moreover, under the effect of infiltration, some $Fe_2Al_{5-x}Zn_x$ grains adjacent to FZ were completely dissociated

from the matrix as shown in Fig. 3(c). With this in mind, the formation mechanism of the interfacial phases is proposed as schematic diagrams provided in Fig. 10.

Firstly, $Fe_2Al_{5-x}Zn_x$ forms at the FZ/steel interface by the diffusion-controlled reaction (Fig. 10a) (Ref 11). Secondly, due to the lower melting point of Zn-22Al filler metal and the excellent infiltration capability of Zn, Zn from liquid FZ starts to infiltrate along $Fe_2Al_{5-x}Zn_x$ GBs driven by interfacial tension forming Zn films. Meanwhile, because of compositional gradient at the FZ/steel interface, solid-state diffusion is triggered. Fe atoms diffuse from steel toward FZ along GBs of $Fe_2Al_{5-x}Zn_x$, and Al atoms diffuse from FZ toward steel along GBs of $Fe_2Al_{5-x}Zn_x$ simultaneously (Ref 27). The elemental diffusion also leads to thickening of the interfacial layer (Fig. 10b). Thirdly, a Fe-deficient zone is likely to form adjacent to FZ side (Fig. 10c). It is because diffusion is a time- and temperature-dependent process. The diffusion distance of Fe atoms is limited on account of rapid cooling during laser joining, which is in contrast to the unlimited infiltration distance of liquid Zn along $Fe_2Al_{5-x}Zn_x$ GBs. As a result, a very few Fe atoms could reach to the $Fe_2Al_{5-x}Zn_x$/FZ interface, leaving a Fe-deficient zone. It then causes strong local variations in composition which would cause nonhomogeneous microstructure. Finally, various processes occur in different zones: In zone I, chemical reactions occur between diffused Fe and Al atoms and Zn films leading to the phase transformation to $FeZn_{10}$ and Al-rich amorphous phase, while in zone II, Zn films along with diffused Al atoms and very few diffused Fe atoms solidified into $Zn_{(ss)}$ (Fig. 10d).

4.2 Toughening Mechanism

As is known to all, the thickness of interfacial layer is very crucial to the joint strength of dissimilar joints. Normally, when the thickness of interfacial layer exceeds a critical value (around 10 μm), the joint strength is likely to be largely reduced. For instance, Dharmendra et al. (Ref 27) reported that the strength of laser Al/steel joint drastically reduced when the thickness of interfacial layer was above 12 μm. However, in the present study, the join strength (peak fracture load) almost keeps constant at 1200 N when the thickness of interfacial layer increases from 20 to 45 μm (Fig. 6). This trend maybe because the interfacial layer was toughened by the soft and tough dispersions.

To elaborate the toughening mechanism, an observation on microindentation cracks in the interfacial phases (zone II) was performed. $Zn_{(ss)}$ were sequentially numbered from No. 1 to No. 3 along the crack propagation direction (Fig. 11). Due to the lower hardness and brittleness of $Zn_{(ss)}$ than $Fe_2Al_{5-x}Zn_x$, the cracks would prefer to generate in $Fe_2Al_{5-x}Zn_x$. With this in mind, the discussion was performed as follows. Initially, the propagating crack suddenly changed the direction as it encountered the phase No. 1, which was because of crack deflection. Then, the phase No. 2 connected two sides of the crack before fracturing, which was due to crack bridging. Finally, the crack was stopped at the phase No. 3 as a result of the completely dissipated energy. This was also a toughening behavior, namely crack arresting. In short, three kinds of toughening behaviors, including crack deflection, crack bridging and crack arresting, were observed. The toughening effect is mainly attributed to the formation of soft and tough $Zn_{(ss)}$ in zone II. Due to the soft and tough nature of $FeZn_{10}$ and Al-rich amorphous phase, the same toughening mechanism can be reasonable expected in zone I. Besides, similar mechanism was reported by Alexander et al. (Ref 28) in the study of A2(Mo,Ti) toughened $C_{14}Fe_2$(Ti, Mo) Laves phase based intermetallic matrix composite. Moreover, because of the toughening effects in the interfacial layer, the fracture are mainly found between interfacial layer and steel, but hardly observed inside the toughened interfacial layer (Fig. 7b).

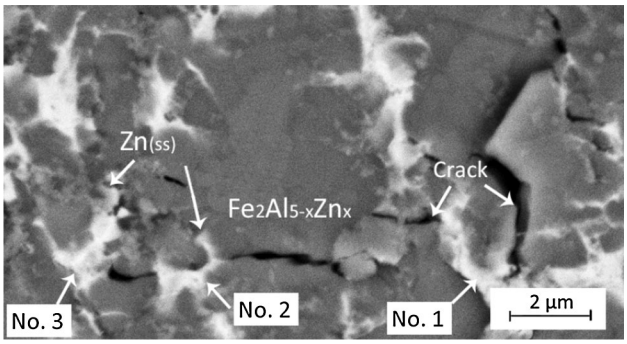

Fig. 11 SEM image of typical microindentation crack showing the $Zn_{(ss)}$ phase numbers

5. Conclusions

By selecting Zn-22Al filler metal as the low-melting-point material and controlling the laser welding process parameters, soft and tough dispersions, i.e., $Zn_{(ss)}$, $FeZn_{10}$ and Al-rich amorphous phase, were successfully produced in the hard and brittle $Fe_2Al_{5-x}Zn_x$ IMCs matrix of dissimilar laser Al/steel joints. Formation mechanism of the dispersions and the associated toughening mechanism were discussed. The major conclusions can be summarized as follows:

1. Formation of the dispersions is resulted from infiltration of liquid Zn and diffusion of elements Al and Fe along $Fe_2Al_{5-x}Zn_x$ GBs and the subsequent chemical reaction and solidification.
2. The interfacial layer is toughed by the soft and tough dispersions, and three toughening behaviors, including crack deflection, crack bridging and crack arresting, are observed.
3. Due to formation of the toughened interfacial layer, the joint exhibits a stable peak fracture load of 1200 N even though the interfacial layer thickness is up to 20-45 μm.
4. The joint shows two failure modes including interfacial failure and fusion zone failure, which are dictated by the geometry of fusion zone rather than the interfacial layer thickness.

Acknowledgments

This work was supported by National Natural Science Foundation of China (Grant Nos. 51265035 and 51375294), and NSERC are gratefully acknowledged. The TEM research was performed at the Canadian Centre for Electron Microscopy at McMaster University, which is supported by NSERC and other

government agencies. One of the authors, Jin Yang, would like to thank Dr. Pan Ma from Shanghai University of Science Engineering for the valuable discussion.

Conflict of Interest

The authors declare that they have no conflict of interest.

References

1. H.T. Fujii, Y. Goto, Y.S. Sato, and H. Kokawa, Microstructure and Lap Shear Strength of the Weld Interface in Ultrasonic Welding of Al Alloy to Stainless Steel, *Scr. Mater.*, 2016, **116**, p 135–138
2. J. Sun, Q. Yan, Z. Li, and J. Huang, Effect of Bevel Angle on Microstructure and Mechanical property of Al/Steel Butt Joint Using Laser Welding-Brazing Method, *Mater. Des.*, 2016, **90**, p 468–477
3. R. Cao, J.H. Sun, J.H. Chen, and P. Wang, Weldability of CMT Joining of AA6061T6 to Boron Steels with Various Coatings, *Weld. J.*, 2014, **93**, p 193s–204s
4. V.K. Patel, S.D. Bhole, and D.L. Chen, Ultrasonic Spot Welding of Aluminum to High-Strength Low-Alloy Steel: Microstructure, Tensile and Fatigue Properties, *Metall. Mater. Trans. A*, 2014, **45**, p 2055–2066
5. P. Prangnell, F. Haddadi, and Y.C. Chen, Ultrasonic Spot Welding of Aluminium to Steel for Automotive Applications-Microstructure and Optimization, *Mater. Sci. Technol.*, 2011, **27**, p 617–624
6. S. Chen, G.S. Daehn, A. Vivek, B. Liu, S.R. Hansen, J. Huang, and S.B. Lin, Interfacial Microstructures and Mechanical Property of Vaporizing Foil Actuator Welding of Aluminum Alloy to Steel, *Mater. Sci. Eng. A*, 2016, **659**, p 12–21
7. Y. Ding, Z. Shen, and A.P. Gerlich, Refill Friction Stir Spot Welding of Dissimilar Aluminum Alloy and AlSi Coated Steel, *J. Manuf. Process.*, 2017, **30**, p 353–360
8. M. Haghshenas, A. Abdel-Gwad, A.M. Omran, B. Gökçe, S. Sahraeinejad, and A.P. Gerlich, Friction Stir Weld Assisted Diffusion Bonding of 5754 Aluminum Alloy to Coated High Strength Steels, *Mater. Des.*, 2014, **55**, p 442–449
9. Y. Huang, J. Wang, L. Wan, X. Meng, H. Liu, and H. Li, Self-Riveting Friction Stir Lap Welding of Aluminum Alloy to Steel, *Mater. Lett.*, 2016, **185**, p 181–184
10. L. Tricarico, R. Spina, D. Sorgente, and M. Brandizzi, Effects of Heat Treatments on Mechanical Properties of Fe/Al Explosion-Welded Structural Transition Joint, *Mater. Des.*, 2009, **30**, p 2693–2700
11. J. Yang, Y.L. Li, H. Zhang, W. Guo, D.C. Weckman, and Y. Zhou, Dissimilar Laser Welding/Brazing of 5754 Aluminum Alloy to DP 980 Steel: Mechanical Properties and Interfacial Microstructure, *Metall. Mater. Trans. A*, 2015, **46**, p 5149–5157
12. J. Sun, J. Huang, Q. Yan, and Z. Li, Fiber Laser Butt Joining of Aluminum to Steel Using Welding-Brazing Method, *Int. J. Adv. Manuf. Technol.*, 2016, **85**, p 2639–2650
13. M.J. Zhang, G.Y. Chen, Y. Zhang, and K.R. Wu, Research on Microstructure and Mechanical Properties of Laser Keyhole Welding-Brazing of Automotive Galvanized Steel to Aluminum Alloy, *Mater. Des.*, 2013, **45**, p 24–30
14. J. Yang, Z. Yu, Y. Li, et al., Influence of Alloy Elements on Microstructure and Mechanical Properties of Al/Steel Dissimilar Joint by Laser Welding/Brazing, *Weld. World,* 2017, p 1–7
15. G. Sierra, P. Peyre, F.D. Beaume, D. Stuart, and G. Fras, Steel to Aluminium Braze Welding by Laser Process with Al-12Si Filler Wire, *Sci. Technol. Weld. Join.*, 2008, **13**, p 430–437
16. C. Wang, L. Cui, G. Mi, P. Jiang, X. Shao, and Y. Rong, The Influence of Heat Input on Microstructure and Mechanical Properties for Dissimilar Welding of Galvanized Steel to 6061 Aluminum Alloy in a Zero-Gap Lap Joint Configuration, *J. Alloy. Compd.*, 2017, **726**, p 556–566
17. L. Li, H. Xia, C. Tan, and N. Ma, Effect of Groove Shape on Laser Welding-Brazing Al to Steel, *J. Mater. Process. Technol.*, 2018, **252**, p 573–581
18. L. Allegra, R.G. Hart, and H.E. Townsend, Intergranular Zinc Embrittlement and Its Inhibition by Phosphorus in 55 Pct Al-Zn-Coated Sheet Steel, *Metall. Mater. Trans. A*, 1983, **14**, p 401–411
19. B.B. Straumal, X. Sauvage, B. Baretzky, A.A. Mazilkin, and R.Z. Valiev, Grain Boundary Films in Al-Zn Alloys After High Pressure Torsion, *Scr. Mater.*, 2014, **70**, p 59–62
20. B.B. Straumal, O.A. Kogtenkova, A.S. Gornakova, V.G. Sursaeva, and B. Baretzky, Grain Boundary Faceting–Roughening Phenomena, *J. Mater. Sci.*, 2016, **51**, p 382–404
21. J. Yang, Y.L. Li, H. Zhang, W. Guo, and Y. Zhou, Control of Interfacial Intermetallic Compounds in Fe-Al Joining by Zn Addition, *Mater. Sci. Eng. A*, 2015, **645**, p 323–327
22. G. Reumont, J.B. Vogt, A. Iost, and J. Foct, The Effects of an Fe-Zn Intermetallic-Containing Coating on the Stress Corrosion Cracking Behavior of a Hot-Dip Galvanized Steel, *Surf. Coat. Technol.*, 2001, **139**, p 265–271
23. M. Windmann, A. Röttger, and W. Theisen, Formation of Intermetallic Phases in Al-Coated Hot-Stamped 22MnB5 Sheets in Terms of Coating Thickness and Si Content, *Surf. Coat. Technol.*, 2014, **246**, p 17–25
24. J.L. Song, S.B. Lin, C.L. Yang, C.G. Ma, and H. Liu, Spreading Behavior and Microstructure Characteristics of Dissimilar Metals TIG welding–Brazing of Aluminum Alloy to Stainless Steel, *Mater. Sci. Eng. A*, 2009, **509**, p 31–40
25. C.W. Lee, D.W. Fan, R. Sohn, S.J. Lee, and B.C. Cooman, Liquid-Metal-Induced Embrittlement of Zn-Coated Hot Stamping Steel, *Metall. Mater. Trans. A*, 2012, **43**, p 5122–5127
26. C.S. Smith, Grains, Phases and Interfaces: an Interpretation of Microstructure, *Trans AIME*, 1948, **175**, p 15–51
27. C. Dharmendra, K.P. Rao, J. Wilden, and S. Reich, Study on Laser Welding-Brazing of Zinc Coated steel to Aluminum Alloy with a Zinc Based Filler, *Mater. Sci. Eng. A*, 2011, **528**, p 1497–1503
28. A.J. Knowles, A. Bhowmik, S. Purkayastha, N.G. Jones, F. Giuliani, W.J. Clegg, and H.J. Stone, Laves Phase Intermetallic Matrix Composite in Situ Toughened by Ductile Precipitates, *Scr. Mater.*, 2017, **140**, p 59–62